Characterization of bimetallic NaY-supported Pt–Pd catalyst by EXAFS, TEM and TPR

Tatjana Rades [a], Chanho Pak [b], Michèle Polisset-Thfoin [a], Ryong Ryoo [b] and Jacques Fraissard [a]

[a] *Laboratoire de Chimie des Surfaces, CNRS URA 1428, Université Pierre et Marie Curie, 4, place Jussieu, T54-55, 75252 Paris Cedex 05, France*
[b] *Department of Chemistry and Center for Molecular Science, Korea Advanced Institute of Science and Technology, Taeduk Science Town, Taejon, Korea*

Received 30 July 1994; accepted 26 August 1994

NaY-supported bimetallic Pt–Pd catalysts have been studied by TEM, TPR and EXAFS. Small, randomly mixed particles are formed in the zeolite cages. When the Pt content is increased, a Pt core structure appears and the dispersion increases. Particle diameters are about 1–2 nm for bimetallic samples.

Keywords: bimetallic catalysts; Pt; Pd; EXAFS; TEM; TPR

1. Introduction

Petrochemistry is based on heterogeneous catalysis using mostly zeolites and supported metals as catalysts. In hydrogenation, dehydrogenation, hydrogenolysis or isomerization of hydrocarbons, but also in the conversion of NO_x, CO (exhaust fumes) and the oxidation of NH_3 [1], platinum- or palladium-based catalysts are the most widely used. In recent years many bimetallic catalysts have been developed and studied.

Few authors have reported negative effects of the second metal in a catalytic system. The presence of Pt in a Ru/SiO_2 catalyst, for instance, inhibits the methanation of CO at the Ru sites [2]. On the other hand, the many advantages of associating two metals requires no further demonstration. The literature gives a good number of examples of such positive interactions as, for instance, improvement in the catalytic activity. The turnover frequency in CH_4–D_2 exchange on a Ru–Pt alloy increases with the Pt percentage [3]. Gold, which is not able to dissociate adsorbed molecules, promotes the reaction between O_2 and H_2 catalysed by Pd [4].

In the case where the activity is not or is only slightly affected by the second metal, the selectivity may be modified by a change of mechanism. A good example is the alloying of gold with platinum (on alumina) which allows hexane isomer-

ization by a "cyclic" mechanism, whereas platinum alone catalyses this reaction by a "bond-shift" mechanism leading to a quite different product distribution [5]. Activity or selectivity changes may proceed from a different surface state or a different dispersion of the metal. Gold, for instance, is known to improve platinum dispersion [6].

Sometimes synergy can be achieved by associating two metals having each indifferent catalytic properties, even if there are only traces of one of them. The conversion of ethanol hydrocarbonylation ethers reaches 48, 24 and 50% for Co, Ru and Rh, respectively, but increases to 53% on Co–Ru and even 70% on Co–Rh alloy [7].

Another significant point is that a second metal may confer resistance to corrosion and poisoning. Pt is often much more reactive than Pd, but it is also more easily poisoned by sulfur or nitrogen compounds, larger amounts of which are present in the heavy petrol cuts. A certain amount of palladium in a platinum catalyst seems to increase its resistance.

Catalyst characterization is very important in catalysis because it explains the chemical, structural and electronic properties of the system. This necessary step may then explain the process which generates the transitional species. Hence it makes it possible to infer the reaction mechanism as well as to give scope for improvements. The important information in heterogeneous catalysis concerns surface properties (structure and composition) at the atomic scale. The most commonly employed characterization techniques are therefore surface techniques like XPS and XRD, followed by infrared spectroscopy and chemisorption. Transmission electron microscopy (TEM) and thermoprogrammed reduction (TPR) are also often used [8]. Other techniques (AES, ESR, NMR, EXAFS, Raman spectroscopy, etc.) may also provide useful information.

In this paper we describe the results of Pd–Pt/NaY catalyst characterization by TPR, by TEM and by EXAFS.

2. Experimental

2.1. PREPARATION

The samples consist of small metal particles supported on an industrial faujasite type NaY zeolite (LZY-54) from UOP (Si/Al = 2.70). All samples were prepared by simultaneous cation exchange by the complexed metal ions ($[Pd(NH_3)_4]^{2+}$ and $[Pt(NH_3)_4]^{2+}$) inspired by the method described by Gallezot et al. [9]. After dissolving appropriate amounts of metal salts, MCl_2 (where M is Pd or Pt), in 250 ml of a 6 M ammonia solution at 80°C, 2.5 g of zeolite is added in order to obtain 0.6 mmol of metal per gram of raw zeolite (equivalent to 6 or 10.5% w/w for the Pd- or Pt-loaded zeolite, respectively). The slurry is stirred for 24 h at 80°C, filtered and thoroughly washed in distilled water to eliminate chloride ions. After drying, the sample is calcined in oxygen with a flow-rate of about 6 ℓ/h, the temperature increasing linearly from RT to T_c = 300°C (temperature gradient = 24°C/h) and

held at T_c for 5 h. T_c was chosen in order to obtain free M^{2+} ions [10,11]. The sample is then purged for 1 h under Ar flow (6 ℓ/h) at 300°C and reduced at 300°C under H_2 flow (6 ℓ/h) for 2 h.

The total number of metal atoms being constant, samples are identified by the relative atom percent of platinum, z, rounded to the nearest multiple of 5% and noted Pt_z. We have also calculated the average number of Pd and Pt atoms per unit cell, x and y respectively, with $x + y = 9.2$–9.9. The weight percent of Pd and Pt (obtained from chemical analysis), relative atom percent as well as the numbers of metal atoms per unit cell are reported in table 1.

2.2. SAMPLE CHARACTERIZATION

For EXAFS measurements, 200–250 mg of the powder sample was pressed into a self-supporting 10 mm diameter wafer. The sample was reduced again in flowing H_2 at 573 K using a Pyrex U-tube flow reactor, transferred to a connected EXAFS cell with Kapton (Du Pont, 125 μm) windows and sealed off under H_2. The EXAFS was measured in the transmittance detection mode at the Pt L_{III} and the Pd K edges at room temperature, using Beam Line 10B at the Photon Factory in Tsukuba. A Si(311) channel cut monochromator was used. The resolutions ($\Delta E/E$) were 1×10^{-4} at the Pt L_{III} edge and 2.5×10^{-4} at the Pd K edge. The X-ray energies for Pt and Pd EXAFS were increased by 2.2 and 2.5 eV steps, respectively. The X-ray intensity was measured by using gas ionization chambers. Analysis of X-ray absorption data was carried out by standard methods [12] using the UWXAFS 2.0 program package distributed by the University of Washington.

Transmission electron microscopy, a widely used method, was carried out with a Jeol JEM 100 CX II apparatus. Resolution was 0.3 nm and the spherical aberration factor C_s 0.7 mm. The zeolite was cut into 80 nm thick sections to allow electron transmission in order to distinguish between metal clusters inside and outside the zeolite grain. The direct picture of the supported metal particles is employed to determine the particle size distribution and then the metal dispersion.

Temperature programmed reduction was performed in a microflow reactor with 300 mg of sample. After the calcination step described above the reactor was

Table 1
Metal content of samples

Sample	% w/w Pd	% w/w Pt	Relative atom% Pt	Pd atoms per unit cell	Pt atoms per unit cell
Pt_{100}	–	10.49	100	0.0	9.2
Pt_{75}	1.45	8.27	75.7	2.3	7.2
Pt_{50}	3.13	5.71	49.9	4.9	4.9
Pt_{25}	4.76	3.00	25.6	7.4	2.5
Pt_0	6.12	–	0	9.4	0.0

slowly cooled to RT in argon flow. Noxal (7 ml/min 5% H_2–95% Ar from Air Liquide) was then allowed to flow through the sample and H_2 consumption detected with a thermal conductivity detector. The temperature was increased linearly from RT up to 650°C at the rate of 600°C/h.

3. Results and discussion

3.1. EXTENDED X-RAY ABSORPTION FINE STRUCTURE (EXAFS)

EXAFS oscillation ($\chi(k)$) was multiplied by the cube of the wave vector (k^3) after background removal and normalization. Figs. 1 and 2 show the $k^3\chi(k)$ and Fourier transforms, which were performed from the region of $2.6 < k < 12.5$ Å^{-1} and $2.9 < k < 13.5$ Å^{-1} for Pd and Pt EXAFS, respectively. Small peaks around 2.1 Å in figs. 1 and 2 are similar to those reported by Toshima et al. [13] for polymer-protected Pt–Pd clusters. These peaks came from a non-linear k-dependence of the phase shift and low-frequency variation in the backscattering amplitude function [14]. The metal–metal first-shell peaks were those in the area of 1.7–3.2 Å (before the phase shift was corrected). The first-shell peak in fig. 1 shifted continuously from 2.52 to 2.67 Å as the mole% of Pt increased from Pt_0 to Pt_{75}. The first-shell peak position in fig. 2 also increased from 2.64 to 2.79 Å as the Pt mole% was changed from 25 to 50. Interestingly, the peak position decreased to 2.76 Å as the Pt content increased further to Pt_{75}. These changes in EXAFS with the Pt/Pd ratio are a qualitative indication of the formation of bimetallic Pt–Pd clusters.

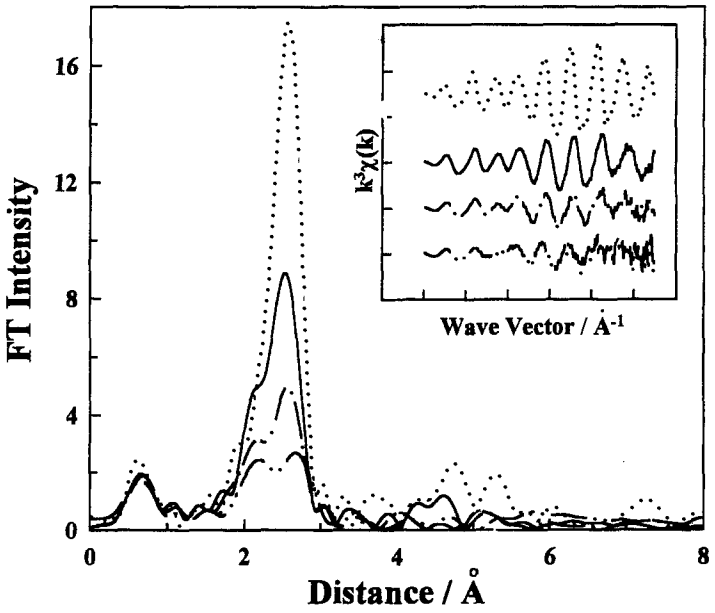

Fig. 1. Fourier transforms of $k^3\chi(k)$ which is shown in inset at the Pd K edge: Pt_0 (- - -), Pt_{25} (——), Pt_{50} (– · –) and Pt_{75} (– ·· –).

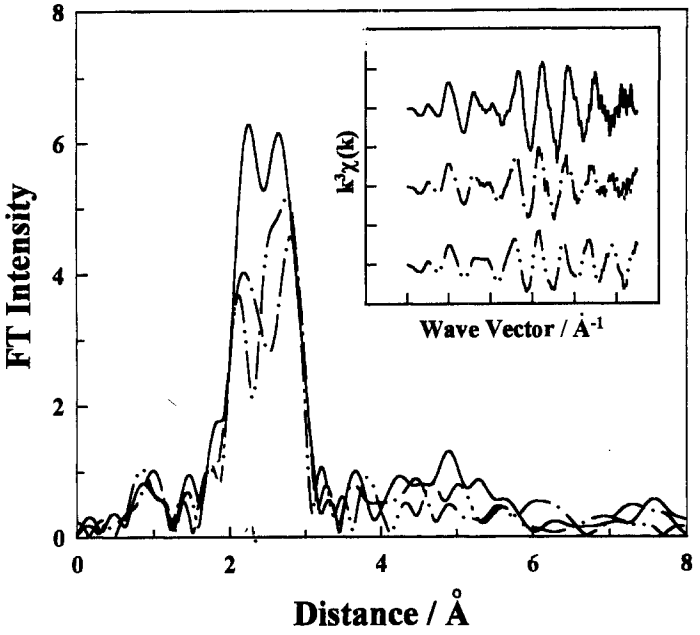

Fig. 2. Fourier transforms of $k^3\chi(k)$ which is shown in inset at the Pt L_{III} edge: Pt_{25} (——), Pt_{50} (– · –) and Pt_{75} (– ·· –).

The Pd EXAFS Fourier transforms in fig. 1 were inverse Fourier transformed to the k space from $1.7 < R < 3.2$ Å, to given a Fourier-filtered EXAFS oscillation such as shown in fig. 3. Similarly, the Pt data in fig. 2 were inverse Fourier transformed for $1.8 < R < 3.2$ Å. Curve-fitting for the Fourier-filtered $k^3\chi(k)$ was performed by using experimental spectra for Pd–Pd and Pt–Pt pairs obtained from metal foils and theoretically calculated spectra for Pt–Pd and Pd–Pt pairs generated with FEFF code [15], under the constraint that the interatomic distances of

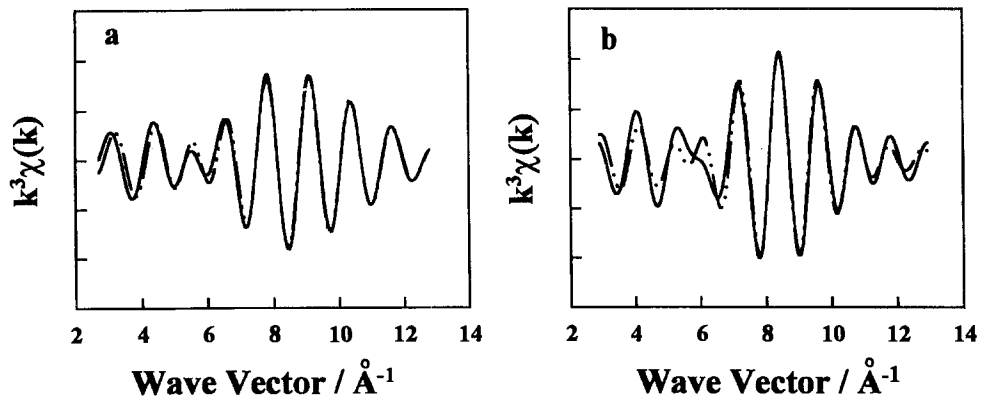

Fig. 3. Fourier-filtered EXAFS spectrum (——) and best fit curve (– ·· –) of Pt_{50} at (a) Pd K and (b) Pt L_{III} edges.

Pd–Pt and Pt–Pd should be equal [16,17]. The curve-fitting results are shown in fig. 3 and the structural parameters obtained by curve-fitting are listed in table 2.

In table 2, the coordination number $N_{M-M'}$ is defined as the number of the nearest-neighbour M′ atoms around M. N_M is the sum for all neighbour metal atoms around M. N_{total} is an average metal coordination number defined for the metal cluster as $N_{Pd}W_{Pd} + N_{Pt}W_{Pt}$, where W_M is the atom percent of M. The coordination numbers in table 2 satisfy the condition for equal coordination of Pt–Pd and Pd–Pt, $N_{Pt-Pd}W_{Pt} = N_{Pd-Pt}W_{Pd}$, within the error limit. The Pt and Pd atoms were also significantly coordinated to each other. Furthermore, very similar values of N_{total}, N_{Pd} and N_{Pt} for Pt_{25} indicate uniform mixing of Pt and Pd atoms in the cluster. As the Pt mole% increased, the ratio of N_{Pt} to N_{Pd} became progressively greater (N_{Pt}/N_{Pd} is 1.1, 1.3 and 1.6 for Pt_{25}, Pt_{50} and Pt_{75}, respectively), indicating that the cluster core became rich in Pt. N_{total} increased from 6.3 to 10 as the Pt

Table 2
Structural parameters of Pd–Pt/NaY catalysts from Pd K edge and Pt L_{III} edge EXAFS

Sample	Absorber	Backscatterer	Distance [a] (Å)	$N_{M-M'}$ [b]	N_M [c]
Pt_0	Pd	Pd	2.82	10.0	
Pt_{25}	Pd	Pd	2.77	5.5	$N_{Pd} = 7.4$
	Pd	Pt	2.76	1.9	
	Pt	Pd	2.76	5.3	$N_{Pt} = 7.8$
	Pt	Pt	2.80	2.5	
			N_{total} [d] = 7.5		
			ΔE_0 [e] = −1 eV		
Pt_{50}	Pd	Pd	2.78	3.7	$N_{Pd} = 6.4$
	Pd	Pt	2.78	2.7	
	Pt	Pd	2.78	4.2	$N_{Pt} = 8.3$
	Pt	Pt	2.81	4.1	
			N_{total} [d] = 7.4		
			ΔE_0 [e] = −2 eV		
Pt_{75}	Pd	Pd	2.80	1.4	$N_{Pd} = 4.4$
	Pd	Pt	2.79	3.0	
	Pt	Pd	2.79	3.6	$N_{Pt} = 6.9$
	Pt	Pt	2.80	3.3	
			N_{total} [d] = 6.3		
			ΔE_0 [e] = 0 eV		

[a] Distance between absorber and backscatterer with ±1% error.
[b] The number of nearest neighbour M′ atom around M with ±15% error.
[c] The sum for all neighbour metal atoms around M.
[d] Average metal coordination number defined for the metal cluster as $N_{total} = N_{Pd}W_{Pd} + N_{Pt}W_{Pt}$, where W_M is atom percent of M.
[e] Adjustment parameter for phase shift which was taken from the condition that the distances of Pd–Pt and Pt–Pd pairs are the same.

mole% decreased from 75 to 0. This increase in cluster size is consistent with the difficulty of preparing small Pd clusters in NaY zeolite [18].

The total coordination numbers for our Pt–Pd cluster, N_{total}, should be equal to $(\sum_{j=1}^{j=12} jN_j)/N_T$, where N_j is the number of atoms with j neighbours and N_T the total number of atoms in the cluster. In the case of cubooctahedral clusters with fcc structure, the cluster size with N_T atoms follows the equation $d_o = 1.105\sqrt[3]{N_T}$ [19], where d_o is the diameter of the equivalent sphere. Combining these two equations, we obtained a graphical relationship between N_{total} and N_T, and used it to find particle diameters which are reported in table 3. The bimetallic clusters seem to be smaller than 1.5 nm.

To summarize, a bimetallic Pt–Pd cluster was formed in NaY zeolite. The size of the bimetallic cluster decreased with the Pt content. The bimetallic cluster changed from a random mixture to a structure with a Pt core as the Pt content increased from 25 to 75%.

3.2. TRANSMISSION ELECTRON MICROSCOPY (TEM)

Particle size distributions were obtained by counting at least 500 particles on several micrographs per sample. Size ranges were chosen so as to fit ruler units on the micrograph enlargement. Cluster size distribution is shown in the form of histograms in fig. 4. The greatest contribution is found between 1.3 and 2.5 nm for all bimetallic samples having between 14 and 41% of particles smaller than 1.3 nm and no particles larger than 5 nm. The histograms also show that the particle diameter increases with the Pd content, but, whereas Pt_{75}, Pt_{50} and Pt_{25} are very similar, Pt_0 has particles with a quite different distribution up to 10 nm around an average diameter of 5.8 nm. Comparison of bimetallic samples with the corresponding TPR-reduced samples showed much larger particles for the latter (>5 nm), which confirms that the particle size depends markedly on preparation and treatment (calcination and reduction).

These statistical data give an apparent diameter without taking into account the particle volume. To have a more compact result than a histogram we calculated an average diameter, d_{TEM}, as reported in table 3.

It is well known that it is difficult to distinguish very small particles (<1 nm) from the zeolite background because of the lack of contrast. We may therefore

Table 3
Average diameter of metal clusters (nm)

	Sample			
	Pt_{75}	Pt_{50}	Pt_{25}	Pt_0
$d_{TEM} = \frac{\Sigma n_i d_i}{\Sigma n_i}$ (nm)	1.5	1.7	1.9	5.8
d_{EXAFS} (nm)	0.8	1.0	1.1	2.5

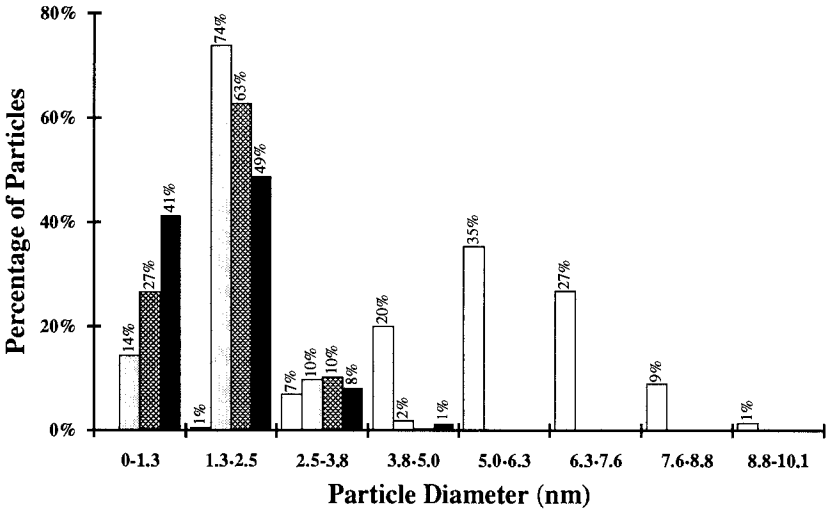

Fig. 4. Particle size distribution of bimetallic Pt–Pd/NaY and monometallic Pd/NaY catalysts obtained from TEM. (□) Pt_0, (▤) Pt_{25}, (▩) Pt_{50}, (■) Pt_{75}.

assume that the number of very small clusters is underestimated by TEM and that this leads to an overestimation of the average diameter, d_{TEM}. The cluster size from EXAFS was significantly smaller than that from TEM, as shown in table 3. A similar difference between the results from EXAFS and TEM, due to an underestimation of the coordination number in the case of very small clusters, was reported for ruthenate and copper particles supported on silica [20,21]. A study of Pt clusters supported on Y zeolite compared diameters deduced from ^{129}Xe-NMR and EXAFS and again found EXAFS results too small [22]. It has also been argued that anharmonic effects in small particles can lead to the coordination number from EXAFS being underestimated [23]. If we therefore consider that cluster sizes are overestimated by TEM but are underestimated by EXAFS, the mean particle sizes should be somewhere in the hatched area of fig. 5, which is the graphical representation of table 3. Further work is necessary to clarify this discrepancy.

The average diameter is an important tool in catalyst characterization. Nevertheless, as surface properties are likely to change with the particle size, one has to take into account the diameter distribution, which may be very different from one sample to another.

3.3. TEMPERATURE PROGRAMMED REDUCTION (TPR)

Experiments at different temperatures showed that the preliminary calcination step considerably affects the metal reduction, modifying the particle size or location in the zeolite structure [24]. This calcination step is necessary for the destruction of the ammonia complex which should be complete from 300°C upwards [11]. We therefore chose a calcination temperature of 300°C both for TPR experiments

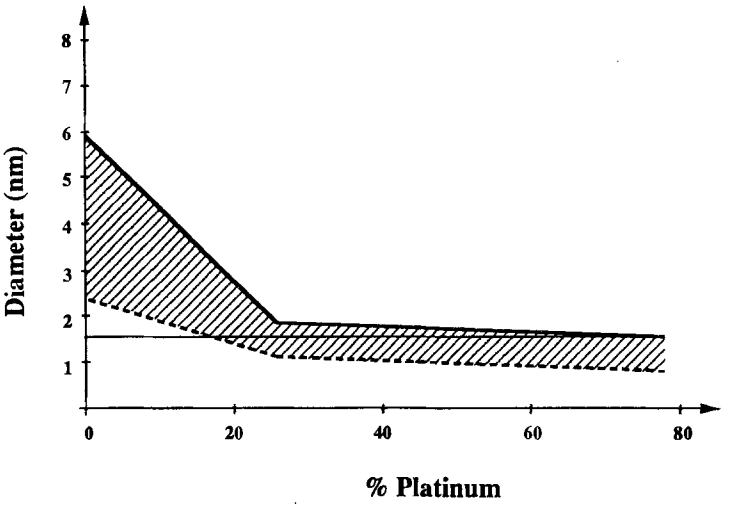

Fig. 5. Particle size in bimetallic Pt–Pd/NaY catalysts as determined by TEM (——) and EXAFS (- - -).

and for mild reduction leading to catalyst elaboration. Moreover, increasing the temperature during calcination favours migration of the decomplexed, and thus smaller, metal cations from the exchange sites (supercages) to the sodalite cages where the metal cation is well coordinated thanks to favorable geometry and high electron density [11].

Reduction of the same metal ion stabilized by these coordination effects is likely to be more difficult than on an amorphous support and should therefore take place at a higher temperature. Thus, the reduction temperature should be strongly dependent on the environment of the ion and we may expect a TPR profile to show as many maxima as there are reduction sites.

Another important aspect of the calcination step is the removal of the decomplexed ammonia as well as of water and any impurities introduced during the preparation step.

The temperature programmed reduction profiles for monometallic samples are shown in fig. 6. Peak temperatures are reported in table 4. The negative parts in the TPR profiles are due to hydrogen desorption. The temperatures of the peaks are determined to within 10–15°C.

In the case of palladium, hydrogen consumption is expressed by a well resolved two-peak profile. The low-temperature peak (LT) appears with a maximum at about 250°C and the high-temperature peak (HT), which is much more important, at 430°C. Platinum reduction, on the other hand, presents an asymmetric signal which can be decomposed mathematically into two peaks of different magnitude having maxima at about 230 and 345°C. With platinum, the importance of the two peaks is reversed, the LT peak being much bigger than the HT peak.

As explained above and as was shown in ref. [25], the fact that there are two peaks would indicate two kinds of reduction sites. Reduction may occur wherever

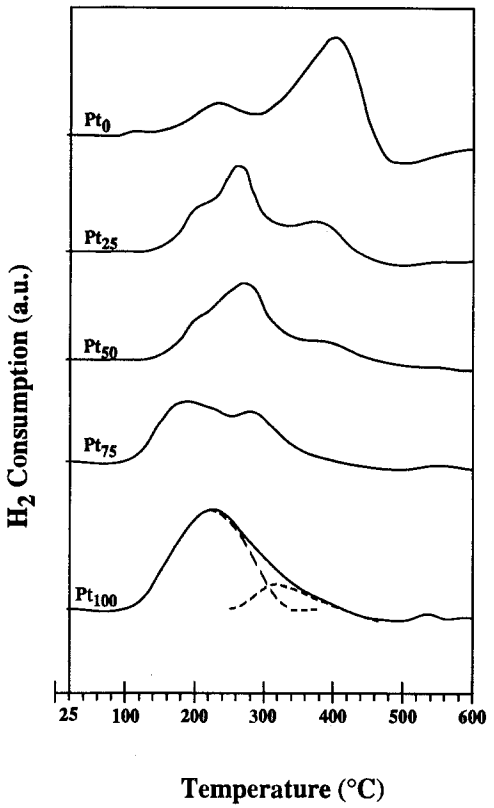

Fig. 6. Reduction profiles of mono- and bimetallic Pt–Pd/NaY catalysts obtained from TPR with 7 ml/min Noxal (5% H_2–95% Ar) flow and a temperature gradient of 600°C/h.

we can find metal ions after calcination, for example in the supercages, in the sodalite cages or in the hexagonal prisms.

We could also imagine that reduction takes place at the zeolite surface. In this case, the ions would have the same reduction properties as if they were reduced on an amorphous support like silica. We therefore compared TPR profiles of zeolite- and silica-supported Pd and Pt: under the same conditions of calcination and reduction, silica-supported Pt and Pd showed a single peak at ~ 240°C and ~ 165°C, respectively [26]. In the case of palladium, the coordination effect is particularly important and the reduction temperatures are very different on zeolite and on

Table 4
Temperatures of TPR maxima for low (LT), medium (MT) and high temperature (HT) peaks in °C, uncertainty of 10–15°C

Peak	Pt_{100}	Pt_{75}	Pt_{50}	Pt_{25}	Pt_0
LT	230	204	216	222	250
MT	–	304	290	281	–
HT	345	(430?)	437	407	430

silica. The existence of two peaks then leads to the conclusion that there are two reduction sites inside the zeolite structure. In the case of Pt, however, which is reduced at low temperatures on both supports, we cannot reach a conclusion without the help of TEM results. The latter show very few metal particles outside the zeolite grains. Moreover, we should expect a similar behaviour for Pt and Pd cations, both divalent and having almost the same diameter. The reduction sites should then be the same. We think that therefore the two reduction sites are situated in the zeolite cages for both Pd and Pt.

According to Homeyer et al. [11] two opposite driving forces arise in the different steps of catalyst preparation. The first one is the already mentioned migration of the cations into the sodalite cages. The reduction step, however, leads to an opposite driving force which is due to the formation of metal–metal bonding. Reduced metal atoms are not stabilized by the negative environment in the cages but by metal–metal bonding. Metal atoms are therefore likely to leave sodalite cages and to migrate into the supercages until they come in contact with other metal atoms.

The TPR profile (fig. 6) for a bimetallic Pd–Pt sample always shows three peaks. Pt_{25} has a first peak at about 222°C, which is a shoulder of the second one at 281°C. A third, but smaller and broader, peak appears at around 407°C. The reduction profile for Pt_{50} is very similar to that of Pt_{25} with maxima at 216, 290 and 437°C. The second peak is smaller than in the Pt_{25} profile but also broader. The HT peak, however, has obviously decreased. In the case of Pt_{75}, the first peak (LT) appears around 204°C and is significantly bigger than the second one at 304°C as well as the LT peaks of Pt_{25} and Pt_{50}. The third peak has almost disappeared, a small residual peak remaining at about 430°C.

We may infer from the monometallic profiles that the third, less important, peak seen above 400°C is probably due to Pd reduction, as it corresponds to the characteristic HT Pd peak. By comparing the bimetallic TPR profiles to each other, we observe an important and non-proportional decrease of this characteristic HT Pd peak when the Pt content increases, though most of the Pd is reduced at 430°C in the monometallic sample.

The first of the remaining two peaks, at about 215°C, may be attributed to Pt reduction but the second, at about 290°C, exists only in bimetallic samples and increases with the Pd concentration. At the same time it shifts slightly from 304 to 281°C when the Pt content decreases from 75 to 25%.

The obvious difference between mono- and bimetallic TPR profiles and the decrease in the HT peak area with increasing Pt content can be taken as a strong indication of alloy formation [27]. Pd seems to be reduced more easily in the presence of Pt, as shown by the marked decrease in the HT Pt peak. To understand this phenomenon we can consider either that Pd and Pt ions coexist in the same reduction sites or that long-distance hydrogen spillover occurs from Pt^0 particles to Pd ions located elsewhere in the zeolite structure [28]. The first hypothesis seems to be confirmed by the EXAFS results which show mixed particles. Spillover, however, is likely to take place at high temperatures.

It is therefore probable that the mechanism for reduction is what some authors call "autocatalysis". Pt ions at the same site as Pd ions (normally reduced at 400°C) start to chemisorb hydrogen as soon as the first Pt^0 atoms appear. Chemisorbed hydrogen, which is dissociated and therefore much more reactive than molecular H_2, is able to reduce Pd with less energy, i.e. at a lower temperature. As Pt is reduced first, we should expect clusters with a Pt-rich core. However, if metal atoms are mobile inside the cluster, especially at the reduction temperature, the metal distribution may change and the system with the lowest surface energy and the highest interatomic energy should appear. EXAFS experiments showed that Pd is located at the cluster surface in one sample (Pt_{75}) but is randomly mixed with Pt in the others, and hence confirm this hypothesis.

4. Conclusion

We have studied five samples of NaY-supported mono- and bimetallic Pt–Pd catalysts by TEM, TPR and EXAFS. Metal was introduced into the zeolite by cation exchange.

TPR reduction profiles showed that the two metals are reduced in the zeolite cages and not on the surface of the zeolite grains. Furthermore, the obvious difference between the monometallic and the bimetallic reduction profiles indicates that mixed particles are formed.

EXAFS confirmed the existence of small bimetallic particles. In addition, EXAFS showed that Pd and Pt are randomly mixed. The sample with strong Pt content (75%), however, has a Pt core structure, according to EXAFS measurements. From the average total coordination numbers we calculated diameters of about 1 nm for bimetallic samples. The particle size of pure Pd catalyst was 2.5 nm.

TEM showed average diameters of less than 2 nm for bimetallic samples and of 5.8 nm for the monometallic Pd sample. Dispersion decreases, as could be expected, with increasing Pd content. As EXAFS underestimates particle sizes in the case of very small particles and as TEM overestimates the average particle diameter these results are coherent. TEM also confirmed the TPR results in showing that all particles are found inside the zeolite grains.

Acknowledgement

We acknowledge partial support for this research from the Photon Factory (Proposal No. 92G193) and Pohang Accelerator Laboratory. Special thanks to M. Lavergne who provided us with beautiful micrographs.

References

[1] M.S. Tzou, K. Asakura, Y. Yamazaki and H. Kuroda, Catal. Lett. 11 (1991) 33.
[2] D.K. Chakrabarty, K.M. Rao, N. Sundararaman and K. Chandavar, Appl. Catal. 28 (1986) 69.

[3] H. Miura, Y. Ushikubo, K. Sugiyama and T. Matsuda, React. Kinet. Catal. Lett. 32 (1986) 487.
[4] Y.L. Lam, J. Criado and M. Boudart, Nouv. J. Chimie 1 (1977) 461.
[5] A. O'Cinneide and F.G. Gault, J. Catal. 37 (1975) 311.
[6] D. Rouabah and J. Fraissard, J. Catal. 144 (1993) 30.
[7] G. Jenner, G. Bitsi and P. Andrianary, Appl. Catal. 24 (1986) 319.
[8] J.W. Niemantsverdriet, in: *Studies in Surface Science and Catalysis*, Vol. 79, eds. J.A. Moulijn, P.W.N.M. van Leeuwen and R.A. van Santen (Elsevier, Amsterdam, 1993) ch. 10.
[9] P. Gallezot, A. Alarcon-Diaz, J.-A. Dalmon, A.J. Renouprez and B. Imelik, J. Catal. 39 (1975) 334.
[10] M.S. Tzou, B.K. Teo and W.M.H. Sachtler, J. Catal. 113 (1988) 220.
[11] S.T. Homeyer and W.M.H. Sachtler, J. Catal. 117 (1989) 91.
[12] B.K. Teo, *EXAFS: Basic Principles and Data Analysis* (Springer, Berlin, 1986).
[13] N. Toshima, M. Harada, T. Yonezawa, K. Kushihashi and K. Asakura, J. Phys. Chem. 95 (1991) 7448.
[14] D.C. Koningsberger and R. Prins, *X-ray Absorption Principles. Applications, Techniques of EXAFS, SEXAFS and XANES* (Wiley, New York, 1988).
[15] J.J. Rehr, J. Mustre de Leon, S.I. Zabinsky and R.C. Albers, J. Am. Chem. Soc. 113 (1991) 5135.
[16] G.H. Via, K.F. Drake Jr., G. Meitzner, F.W. Lytle and J.H. Sinfelt, Catal. Lett. 5 (1990) 25.
[17] R. Ryoo, C. Pak and S.J. Cho, *Proc. 7th Int. Conf. on XAFS*, Kobe, August 1992, Japan J. Appl. Phys. 32 (1993) 475.
[18] J.-G. Kim, S.-K. Ihm, J.Y. Lee and R. Ryoo, J. Phys. Chem. 95 (1991) 8546.
[19] R. van Hardeveld and F. Hartog, Surf. Sci. 15 (1969) 189.
[20] A.T. Ashcroft, A.K. Cheetham, P.J.F. Harris, R.H. Jones, S. Natarajan, G. Sankar, N.J. Stedman and J.M. Thomas, Catal. Lett. 24 (1994) 47.
[21] G. Sankar, J.M. Thomas, D. Waller, J.W. Couves, C.R.A. Catlow and G.N. Greaves, J. Phys. Chem. 96 (1992) 7485.
[22] R. Ryoo, S.J. Cho, C. Pak and J.Y. Lee, Catal. Lett. 20 (1993) 107.
[23] B.S. Clausen, L. Gråbæk, H. Topsøe, L.B. Hansen, P. Stoltze, J.K. Nørskov and O.H. Nielsen, J. Catal. 141 (1993) 368.
[24] M. Polisset, Doctoral Thesis, Universit de Paris VI, France (1990).
[25] S.T. Homeyer and W.M.H. Sachtler, J. Catal. 118 (1989) 266.
[26] M. Polisset and J. Fraissard, to be published.
[27] F.B. Noronha, M. Schmal, M. Primet and R. Frèty, Appl. Catal. 78 (1991) 125.
[28] H. Lieske and J. Völter, J. Catal. 90 (1984) 96.